energies

MDPI

Article

LES and RANS Spray Combustion Analysis of OME_{3-5} and n-Dodecane

Frederik Wiesmann [1,*], Tuan M. Nguyen [2], Julien Manin [2], Lyle M. Pickett [2], Kevin Wan [2], Fabien Tagliante [2] and Thomas Lauer [1]

[1] Institute of Powertrains and Automotive Technology, TU Wien, 1060 Vienna, Austria; thomas.lauer@ifa.tuwien.ac.at

[2] Sandia National Laboratories, 7011 East Ave, Livermore, CA 94551, USA; nguyen147@llnl.gov (T.M.N.); jmanin@sandia.gov (J.M.); lmpicke@sandia.gov (L.M.P.); kwan@sandia.gov (K.W.); tagliante.fabien@gmail.com (F.T.)

* Correspondence: frederik.wiesmann@ifa.tuwien.ac.at; Tel.: +43-1-588-013-1560

Abstract: Clean-burning oxygenated and synthetic fuels derived from renewable power, so-called e-fuels, are a promising pathway to decarbonize compression–ignition engines. Polyoxymethylene dimethyl ethers (PODEs or OMEs) are one candidate of such fuels with good prospects. Their lack of carbon-to-carbon bonds and high concentration of chemically bound oxygen effectively negate the emergence of polycyclic aromatic hydrocarbons (PAHs) and even their precursors like acetylene (C_2H_2), enabling soot-free combustion without the soot-NO_x trade-off common for diesel engines. The differences in the spray combustion process for OMEs and diesel-like reference fuels like n-dodecane and their potential implications on engine applications include discrepancies in the observed ignition delay, the stabilized flame lift-off location, and significant deviations in high-temperature flame morphology. For CFD simulations, the accurate modeling and prediction of these differences between OMEs and n-dodecane proved challenging. This study investigates the spray combustion process of an OME_{3-5} mixture and n-dodecane with advanced optical diagnostics, Reynolds-Averaged Navier–Stokes (RANS), and Large-Eddy Simulations (LESs) within a constant-volume vessel. Cool-flame and high-temperature combustion were measured simultaneously via high-speed (50 kHz) imaging with formaldehyde (CH_2O) planar laser-induced fluorescence (PLIF) representing the former and line-of-sight OH^* chemiluminescence the latter. Both RANS and LES simulations accurately describe the cool-flame development process with the formation of CH_2O. However, CH_2O consumption and the onset of high-temperature reactions, signaled by the rise of OH^* levels, show significant deviations between RANS, LES, and experiments as well as between n-dodecane and OME. A focus is set on the quality of the simulated results compared to the experimentally observed spatial distribution of OH^*, especially in OME fuel-rich regions. The influence of the turbulence modeling is investigated for the two distinct ambient temperatures of 900 K and 1200 K within the Engine Combustion Network Spray A setup. The capabilities and limitations of the RANS simulations are demonstrated with the initial cool-flame propagation and periodic oscillations of CH_2O formation/consumption during the quasi-steady combustion period captured by the LES.

Keywords: CFD; OME; PODE; polyoxymethylene ether; e-fuels; oxygenated fuels; ECN; RANS; LES; spray combustion

Citation: Wiesmann, F.; Nguyen, T.M.; Manin, J.; Pickett, L.M.; Wan, K.; Tagliante, F.; Lauer, T. LES and RANS Spray Combustion Analysis of OME_{3-5} and n-Dodecane. *Energies* **2024**, *17*, 2265. https://doi.org/10.3390/en17102265

Academic Editor: Constantine D. Rakopoulos

Received: 5 April 2024
Revised: 24 April 2024
Accepted: 26 April 2024
Published: 8 May 2024

1. Introduction

Oxygenated synthetic fuels promise to be a viable pathway to significantly reduce the CO_2 footprint of hard-to-decarbonize applications. Concerning the potential of OMEs within engine applications, several studies identified mixtures of OME_{3-5} to be the most suitable alternative for diesel fuel because of the similar viscosity, lubricity, and boiling point, as well as lower volatility and higher cetane number compared to OME_1 [1–3].

Hereby, the chemical structure of OMEs ($CH_3O(\text{-}CH_2\text{-}O)_n\text{-}CH_3$) is characterized by the number of oxymethylene ether groups (CH_2-O) within. According to [4], a greater number of oxymethylene ether groups is beneficial for NO_x emissions and only slightly reduces the thermal efficiency observed in a single-cylinder diesel engine. While Virt and Arnold [5] showed reduced particulate emissions and faster ignition, i.e., shorter ignition delays, for blends of diesel with up to 45 vol.% of OME_{3-5}, Pélerin et al. [6] used a pure OME_{3-6} fuel comparing it to diesel in a heavy-duty engine. It was found that the OME_{3-6} fuel had drastically reduced soot and particulate emissions without increasing emission levels of NO_x, hence effectively mitigating the soot-NO_x trade-off typical for diesel engines. These observations were confirmed for engines fueled with both diesel–OMEs blends [7–10] and neat OMEs [3,11–13].

Besides engine operation aspects, the mixing and combustion characteristics of OMEs are crucial to extracting the fuel's full potential and possibly guiding adaptations to future engine design needed for the widespread usage of OME fuels. Several studies, especially within the framework of the Engine Combustion Network (ECN) [14], worked with the same OME_{3-5} fuel composition used in this study. The macroscopic characteristics of the OME_{3-5} fuel mix compared to OME_1, n-dodecane, and hydrotreated vegetable oil (HVO) were reported in [15] showing a longer liquid length and shorter ignition delay for OME_{3-5} compared to n-dodecane, despite its lower cetane number. The mixing process of OME_{3-5} was analyzed in comparison to n-dodecane and 1-octanol [16]. All fuels proved to have very similar mass distributions, and the differences in equivalence ratio distributions were solely a consequence of the different air requirements for stoichiometric mixing of the oxygenated fuels. Non-reacting as well as ignition characteristics of the OME_{3-5} fuel were studied in [17] within a constant-pressure vessel experimentally and numerically, employing Reynolds-Averaged Navier–Stokes (RANS) calculations. Significant differences to n-dodecane were reported concerning the distribution of high-temperature reaction zones characterized by OH^* chemiluminescence. The RANS calculations, tracking the OH species rather than the excited OH^* radical, were able to depict the trends of higher OH accumulation in the spray symmetry plane for OME. The entire combustion process was shown not to exceed equivalence ratios greater than two for OME, which is, of course, in stark contrast to the combustion of n-paraffinic fuel like n-dodecane. These observations were confirmed for a single-cylinder optically accessible diesel engine in [18] using the same RANS setup and injection strategy and also recently by García-Oliver et al. [19] utilizing a different simulation setup and injection strategy but the same OME fuel. However, the simulations could not reproduce the strong OH^* chemiluminescence signal in the spray center axis and the peak intensity near the flame lift-off length in either the constant-pressure vessel or the single-cylinder engine.

Pastor et al. [20] investigated the combustion characteristics of the OME_{3-5} fuel mixture for the standard operating condition of the ECN [14] using formaldehyde PLIF, signaling the rise of low-temperature reactions, and OH^* chemiluminescence, indicating the onset of the high-temperature flame. The results demonstrated a clear separation of the cool flame and high-temperature reaction zone for one ECN standard injector (Spray A), but also a propagation of CH_2O downstream of the flame lift-off length for a different injector with more than twice the size of the actual nozzle diameter (Spray D). The richer spray in the case of Spray D was assumed to impede the CH_2O consumption at the spray axis.

A recent study by Kaario et al. [21] demonstrated the two-stage ignition characteristics for another oxygenated fuel, namely methanol, using Large-Eddy Simulations (LESs). The simulations showed that the methanol ignition is characterized by a higher heat release rate during the low-temperature chemistry or first-stage ignition and not during the high-temperature reactions, which is opposite to the behavior of classical two-stage ignition phenomena, e.g., for n-dodecane. The first-stage ignition was also shown to occur in a narrow range of temperatures and equivalence ratios for methanol, with its heat release rate two orders of magnitude smaller than that of n-dodecane. It was also demonstrated that n-dodecane has a temporally much more distinct two-stage ignition compared to methanol.

The differences in the transient two-stage ignition for OME fuels and n-dodecane are not yet determined conclusively. The present work aims to leverage numerical models to gain additional insights into the transition of the cool-flame propagation to the high-temperature ignition of an OME_{3-5} fuel mixture. Additionally, previous studies mainly focused on the standard ECN Spray A operating point with an ambient temperature of 900 K at the start of injection. Therefore, the impact of highly elevated ambient temperature on the auto-ignition process and the flame morphology of OME_{3-5} is investigated in the current study. For this, the ability of the constant volume pre-burn chamber at Sandia National Laboratories was utilized to achieve an ambient temperature of 1200 K at the start of fuel injection. The impact of the elevated temperature on the distribution of simulated *OH* and measured *OH** chemiluminescence, especially, were of interest. Another focus of this work is to conduct an in-depth comparative analysis concerning the quality and limitations of the simulated results for RANS and LES calculations to identify possible areas of improvement for both turbulence modeling approaches based on experimental measurement.

First, the impact of highly elevated ambient temperature is described. Secondly, the findings on the cool-flame propagation and transition to high-temperature reactions are presented.

2. Setup

Experiments and simulations were conducted using a common-rail single axial hole piezo injector named Spray A3 with a measured diameter of 94 µm. The injector has a convergent nozzle with a K-factor of 3.2. More details of the injector are referenced in [22].

2.1. Fuels

The multi-component oxymethylene ether fuel mix in the study, from now on simply *OME*, is detailed in its composition of different components by an analysis conducted by Analytik Service Gesellschaft (ASG) [23] shown in Table 1.

The most important physical and chemical properties of n-dodecane, hereinafter simply *DOD*, and OME are given in Table 2 with values taken from the batch report of ASG and from [15]. Additionally, the heat of evaporation derived from the internal AVL FIRE® database at a temperature of 90 °C is shown in Table 2 for both fuels.

Table 1. OME fuel mix.

Molecule	Content [wt%]
OME_1	0.01
OME_2	<0.01
OME_3	57.90
OME_4	28.87
OME_5	10.07
OME_6	1.91

Table 2. Fuel properties for n-dodecane and OME.

Property	Unit	n-Dodecane	OME
Density	kg/m^3 (T = 15 °C)	751.20	1057.10
Viscosity	mm^2/s (T = 40 °C)	1.44	1.08
Cetane number	-	74	68.6
Lubricity	µm	563	320
Flash point	°C	83	65

Table 2. *Cont.*

Property	Unit	n-Dodecane	OME
Lower heating value	MJ/kg	44.20	19.26
Initial boiling point	°C	214.00	144.40
Final boiling point	°C	218	242.4
Total contaminations	mg/kg	-	<1
Carbon content	% [m/m]	84	43
Hydrogen content	% [m/m]	16	8.53
Oxygen content	% [m/m]	0	46.4
$(A/F)_{st}$ at 21% of O_2	-	14.92:1	5.89:1
$(A/F)_{st}$ at 15% of O_2	-	20.72:1	8.18:1
Heat of Vaporization (T = 90 °C)	kJ/mol	62.80 *	52.23 *

* Taken from internal AVL FIRE database.

2.2. Operating Points

The operating points realizing the medium (OP1) and high ambient temperature (OP2) conditions used for the experiments and simulations in this study are shown in Table 3.

Table 3. Operating points.

Name	T_{CC} [K]	p_{CC} [bar]	ρ_{CC} [kg/m^3]	T_{inj} [K]	p_{inj} [bar]	t_{inj} [ms]	O_2-Content [vol.%]
OP1	900	61	22.8	363	1500	1.5	15
OP2	1200	78	22.8	363	1500	1.5	15

2.3. Experimental Setup

Experiments were performed inside an optically accessible constant volume pre-burn chamber at Sandia. The operating conditions can be found in Table 3. Ambient conditions were controlled using a pre-burn technique. Details on the vessel and its operation can be found in previous works and on the ECN website. High-speed planar laser-induced fluorescence (PLIF) imaging of CH_2O was performed using a burst-mode Quasi-Modo Nd:YAG laser operating at 355 nm and 50 kHz. A Semrock multiline CH_2O filter was used for spectral filtering, as well as a 450 nm shortpass filter to attenuate soot incandescence at longer wavelengths. Further details on the PLIF technique can be found in [22] regarding corrections for background luminosity and laser spatial and temporal variations. High-speed OH* chemiluminescence was performed simultaneously with a 308 nm OH* filter and 358 nm shortpass filter. Further details on the OH* technique can be found in [24]. Phantom v2512 high-speed cameras were used for imaging of both diagnostics. The ignition delay was also measured by using a piezoelectric pressure transducer. It was positioned in a lower corner of the vessel, opposite the injector. The pressure measurements were adjusted for the the time delay caused by the speed of sound and the distance from ignition site to pressure transducer according to [25]. Further details can be found on the ECN website [14].

2.4. Numerical Setup

The RANS calculations were carried out with AVL FIRE® R2020.1. LES calculations were performed using CONVERGE 3.0 CFD code.

However, both codes have employed a similar modeling framework using the Lagrangian–Eulerian approach. In this framework, liquid fuels are modeled as stochastic particles in a Lagrangian manner. On the other hand, the gaseous flow field is solved in the traditional Eulerian formulation. The momentum and heat/mass exchange processes between the liquid and gaseous phases are modeled and not resolved. Spray breakup was modeled in all cases by the KH-RT methods [26]. The spray plume cone angle for the simulations was set to 14°, following the results on Spray A near-field measurements in [27].

The liquid injection was realized with the *Blob* method that initializes the liquid parcels with a size corresponding to the actual nozzle exit diameter of the injector. The same methodology to generate the injection rates is employed for all calculations. The publicly available tool from the Polytechnical University of Valencia [28] guarantees a standardized method for numerical studies to create consistent injection rate profiles for the ECN Spray A3 injector. Figure 1 depicts the rates of injections for DOD and OME for an injection pressure of p_{inj} = 1500 bar and for an injection duration of t_{inj} = 1500 µs as stated in Table 3 for the studied operating points.

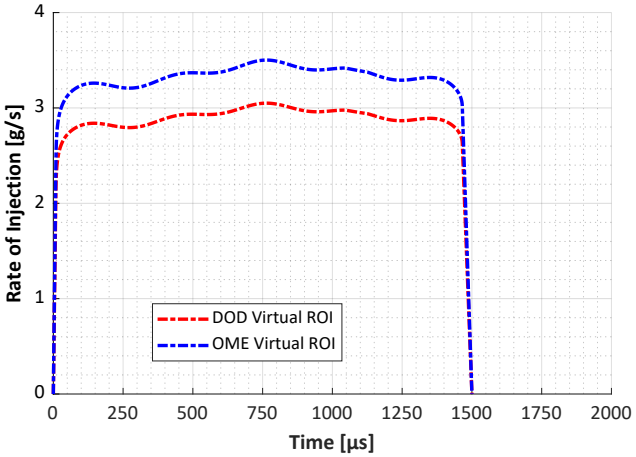

Figure 1. Rates of injection for n-dodecane and OME for Spray A3 injector according to [28].

In all cases, the combustion was modeled using chemical kinetic solvers with the well-stirred reactor assumption for each computational cell using the multi-zone technique. This approach clusters cells with similar thermodynamic conditions (temperature and equivalence ratio). The chemical reactions are solved for the mean of these clusters and the results are mapped back to the respective cells. The clustering and mapping-back procedures are applied according to [29].

A major goal of the current research is to ensure sufficient resolution of the mixture within the turbulent flow field when coupled to a direct chemistry integration approach that avoids mechanism-reduction compromises that alter or de-emphasize cool-flame (CH_2O) prediction. RANS calculations with enabled turbulence chemistry interaction (TCI) were set as benchmark tests and did not show any meaningful differences in global ignition characteristics (ignition delay, flame lift-off length) or flame morphology when compared to simulations using the multi-zone speed-up option. This indicates a well-resolved flow field due to the high grid resolution. Hence, this approach was used for the detailed analysis comparing RANS to LES, as for the latter the multi-zone approach was adopted for keeping the computational time within reasonable limits.

For n-dodecane, a 251-species and 1484-reactions chemical mechanism, developed by the Lawrence Livermore National Laboratory (LLNL) and described in the supplementary material in [24], was used. The OME simulations were carried out with the Niu mechanism [30] consisting of 92 species and 389 reactions. For validation of the used mechanisms regarding ignition delay and laminar flame speeds using 0-D simulations, the reader is referred to the respective reference.

The approach in this current work is to compare our best effort simulations using each institution's respective tool. As shown in this work, these LES and RANS methods have been extensively validated in previous works. Combined with the efforts to match chemical kinetic mechanisms and combustion models, the focus of this work is not only to compare RANS and LES results, but to identify the area of improvements for approaches by performing in-depth analysis grounded by the experimental measurements. The following subsections describe the differences in the modeling setup for the LES and RANS simulations.

2.4.1. LES Setup

The Lagrangian spray and LES turbulence models used in this work have been extensively validated for non-reacting [31] and reacting flow [24]. The parameters for different models are summarized in Table 4.

Both fixed-cell embedding and adaptive mesh refinement (AMR), with the smallest cell size of 62.5 µm, were used to sufficiently resolve both spray and flame dynamics. The fixed-cell embedding region has the shape of 20 mm long cone, centered around the injector axis. Such a fine mesh region is required to adequately resolve both the spray dynamics upstream and the subsequent low-temperature flame downstream of the liquid length. In an attempt to resolve as much as possible the high-temperature flame region, AMR is activated on velocity and temperature gradients, which is most active in the edge flame region downstream of the lift-off length. At steady state, 50 million cells were used in some calculations.

In the fixed embedding region, especially around the flame core where the low-temperature chemistry is the most relevant, less than 20 % of the total kinetic energy has to be modeled. However, more than 20 % of the total kinetic energy has to be modeled in the high-temperature flame region, despite the aggressive AMR strategy. So the overall LES can be considered well resolved, where less than 20 % of the total kinetic energy has to be modeled [32]. The main purpose of the meshing strategy in these LES calculations is to alleviate some weakness associated with the well-stirred reactor model employed in this work. To the authors' best knowledge, these LESs are the finest ones compared to other LESs of Spray A [33–35]. The above discussion provides confidence for the low- and high-temperature flame analysis presented in this work.

2.4.2. RANS Setup

The RANS simulations of this study were conducted on a fixed mesh with a base cell size of 1 mm. Three refinement steps in the near-nozzle area resulted in a minimum cell edge length of 125 µm. Figure 2 visualizes the spray-box mesh with its refinement areas and a cell count of 966,000.

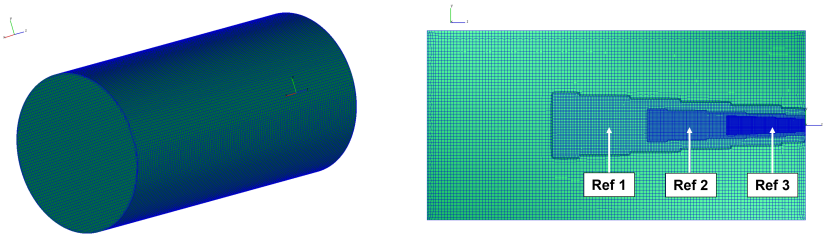

Figure 2. Mesh with refinements in symmetry plane for RANS calculations. The terms Ref 1 to Ref 3 visualize the mesh refinements with Ref 1, Ref 2 and Ref 3 denominating cells with an edge length of 500 µm, 250 µm and 125 µm respectively.

The mesh and the models for the liquid and gaseous phase for the RANS calculations were validated extensively in [17,18]. The validation included a grid independence study, which was conducted for non-reacting as well as reacting conditions. Using a temporal resolution of dt = 0.5 µs, the utilized cell sizes for the RANS computations represent a higher spatial resolution than recommended by the modeling standards of the ECN, which propose a minimum cell size of 250 µm [14]. This way the setup ensures that the liquid droplets evaporate within the highest resolution region of 125 µm and that the subsequent ignition occurs within cells with a maximum edge length of 250 µm. The chosen RANS turbulence model is the k-ζ-f model proposed in [36], which is the further development of the k-$\overline{v^2}$-f model derived by Durbin [37]. This k-$\overline{v^2}$-f model enhances the classic isotropic k-ϵ model [38] by introducing an additional transported variable, the wall-normal velocity scale ($\overline{v^2}$), which is sensitive to the wall-blocking effect and imposes the correct (anisotropic)

kinematic boundary condition on the normal component of the turbulent intensity in near-wall regions of turbulent shear flows via an elliptic relaxation function (f). Hanjalić et al. proposed in [36] to solve not for the velocity scale but rather alternatively for the velocity scale ratio ($\zeta = \overline{v^2}/k$), thus delivering a numerically more robust and efficient model.

The constants for the KH-RT [26] spray breakup model within the RANS setup were set to $B_0 = 0.61$ and $B_1 = 10$. Liquid spray evaporation is modeled with the method of Brenn et al. [39], which accounts for the multiple oxymethylene ether components of the OME fuel.

Table 4. Summary of simulation setup.

Liquid Spray Models	**RANS**	**LES**
Injection type	Blob [40]	
Breakup (KH-RT [26])	$B_0 = 0.61$, $B_1 = 10$	$B_0 = 0.6$, $B_1 = 7$
Turbulent dispersion	O'Rourke [41,42]	
Evaporation	Brenn et al. [39]	Frossling [42] including corrected distortion [31]
Drag Law	Schiller-Naumann [43]	Liu et al. [44] with corrected distortion [31]
Gaseous phase models	**RANS**	**LES**
Maximum cell count	966,000	≈60 million
Minimum grid size	125 µm	62.5 µm
Turbulence modeling	k-ζ-f model [36]	One-equation Dynamic Structure LES model [45]

3. Results and Discussion

LES and RANS calculations adhere to the ECN modeling standards [14] to determine ignition delay and flame lift-off length. Ignition is calculated by identifying the time of the maximum gradient in temperature. The flame lift-off is set to be the axial location closest to the nozzle at which the *OH* mass fraction reaches 14% of its maximum in the computational domain. In the experiments, ignition and flame lift-off length are measured based on *OH** chemiluminescence following a similar procedure to that described in [24]. To summarize, lift-off length is measured using the time-averaged quasi-steady chemiluminescence intensity field to obtain two lobes of high intensity at the top and bottom of the jet near the lift-off length. The ECN defines the lift-off length as the average axial distance between the injector and the first axial locations of the two lobes with an intensity greater than 50%, compared to the leveling-off value. The onset of ignition is measured as the first frame, where 10 pixels reach this same 50% threshold. Additionally, the pressure-based ignition delay was detected by the start of the rapid pressure rise caused by high-temperature ignition.

Figure 3 compares the results for LES, RANS, and experiments for high-temperature ignition delay (ID) and flame lift-off length (LOL) for both operating points. It can be seen that the simulations reproduce the experimental data well in general. However, the LES seems to overestimate the lift-off for n-dodecane in the case of 1200 K ambient temperature and slightly underestimate the lift-off length for OME for 900 K ambient temperature. Remarkably, LES and RANS predict an identical ignition delay for n-dodecane in the case of 900 K ambient temperature, namely 340 µs, which is valuable for being able to compare the transition from the cool-flame to high-temperature combustion for both turbulence modeling approaches.

At first, the influence of the ambient temperature on the high-temperature flame morphology for both fuels will be discussed in Section 3.1. A detailed analysis of the spatial distribution of the measured and simulated hot-flame shapes for 900 K and 1200 K is presented.

Finally, the transient development of the cool flame with a focus on the different combustion stages for n-dodecane and OME is described in Section 3.2.

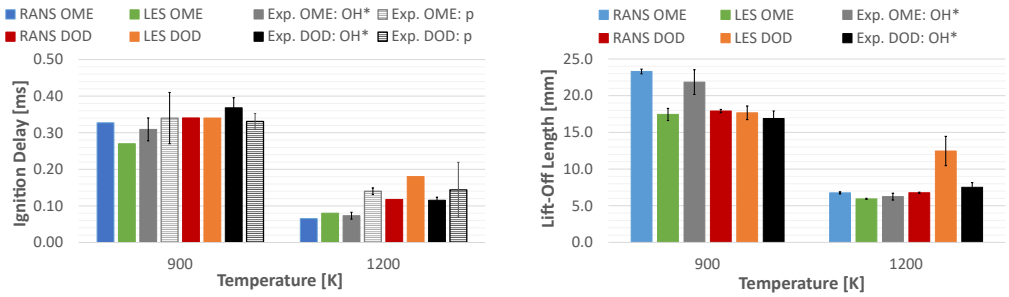

(**a**) Ignition delay. (**b**) Lift-off length.

Figure 3. Simulated versus experimental ignition delay and lift-off length. *OH** describes experimental data based on *OH** chemiluminescence and *p* denotes pressure-based determination of the ignition delay.

3.1. Influence of Ambient Temperature on Hot-Flame Morphology

To interpret the transient evolution of the low- and high-temperature flame in a compact manner, spatiotemporal plots in the form $I_{xt} = \int_{y_{min}}^{y_{max}} c_{CH_2O}(x, y, t)dy$ are shown in Figure 4, with c_{CH_2O} referencing either the measured PLIF intensity or the simulated CH_2O molar concentration, x the axial location, and y the cross-stream radial coordinate. Additionally, *OH** intensity and *OH* molar concentration are plotted into the contour, with the respective intensity and concentration present at the flame lift-off length. The *OH* species was chosen as a simulation reference to the *OH** chemiluminescence experiments because the used OME reaction mechanism does not contain an excited *OH** species. The *OH** chemiluminescence experiments are line-of-sight *OH**. For LES and RANS, the *OH* species mass fractions were first integrated in the normal direction to the visualized plane and then projected onto it. This ensures an accurate comparison.

The most significant difference between the fuels is the complete absence of polycyclic aromatic hydrocarbons (PAHs) for OME, which form for n-dodecane separated in space and time from the detected formaldehyde for $t_{aSOI} \geq 520$ µs and $x > 30$ mm in the case of a 900 K ambient temperature (Figure 4a). Hereby, the normalization of the measured intensity was rendered with the maximum value PLIF intensity before the onset of PAH formation. According to Sim et al. [22], several key PAH molecules are excited by the used 355 nm of the PLIF diagnostic. The main difference between turbulence modeling approaches is that the RANS calculations show a steady distribution of CH_2O in time. The LES is characterized by the cyclic rise and fall of CH_2O concentration as the injection progresses. It is also visible that these oscillations of the LES lead to the formation of CH_2O far upstream compared to the RANS calculations for both fuels. The contours of the cool and hot flame in axial space and time are well represented by both simulations, with the LES showing a slightly better match, at least for the 900 K ambient temperature.

For all realizations, CH_2O is formed after the first ignition stage and then accumulates to its maximum concentration before being consumed by the high-temperature flame. At 900 K ambient temperature, Figure 4a, CH_2O forms well upstream of the lift-off length and shows a significantly high concentration of CH_2O at the location of flame stabilization. This confirms for OME the previous findings for n-dodecane in [24] that CH_2O promotes ignition and helps stabilize the high-temperature flame at the 900 K operating point.

In the case of 1200 K, Figure 4b, the spatial sequence of CH_2O formation and consumption is more challenging to interpret. Experimentally, two factors are affecting the results. For n-dodecane, the formation of PAHs occurs from approximately $t_{aSOI} \geq 160$ µs onwards, which is very soon after the initial formation of CH_2O. Only a small temporal window separates the region of increased PAH yield with the measurement of actual CH_2O intensity. This separation is even absent when considering the axial distance. Starting at $x \geq 13$ mm downstream of the nozzle, PAHs form for n-dodecane. Secondly, the PLIF measurements can only detect signals downstream of the liquid length. The thresholds for the PLIF experiments were set up to a fixed number of 35 counts for all experiments

except for the case of 1200 K ambient temperature (OP2) and using OME as fuel. In that case, only five frame counts were set as thresholds. As the liquid phase of OME penetrates further into the combustion chamber than n-dodecane, as shown in [17], part of the CH_2O formation when using OME as fuel at the 1200 K operating point cannot be captured experimentally. For both fuels, the flame stabilization in Figure 4b occurs upstream of the maximum concentration of CH_2O, which differs from the 900 K case. The periodic oscillations of CH_2O formation and consumption are also present for the LES in the case of 1200 K ambient temperature.

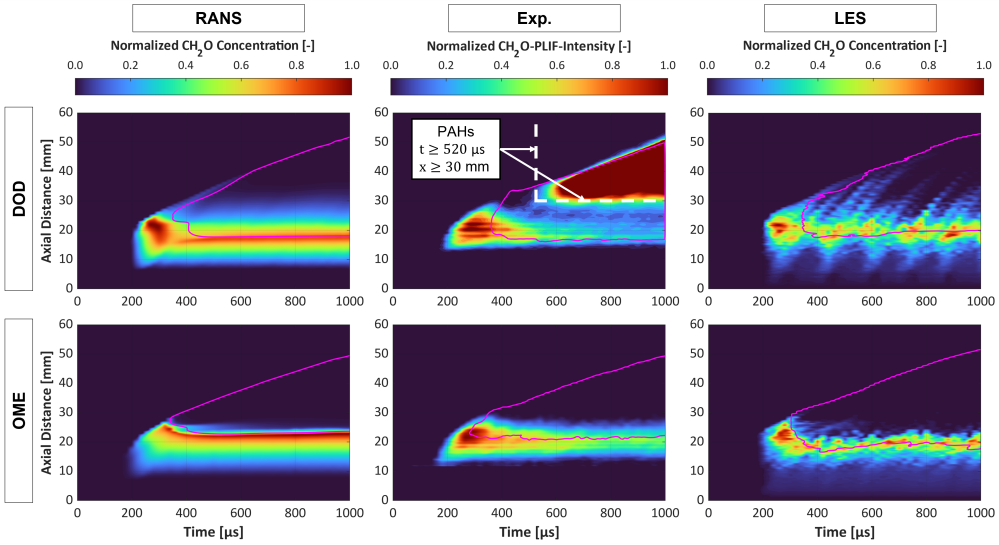

(**a**) OP1: 900 K

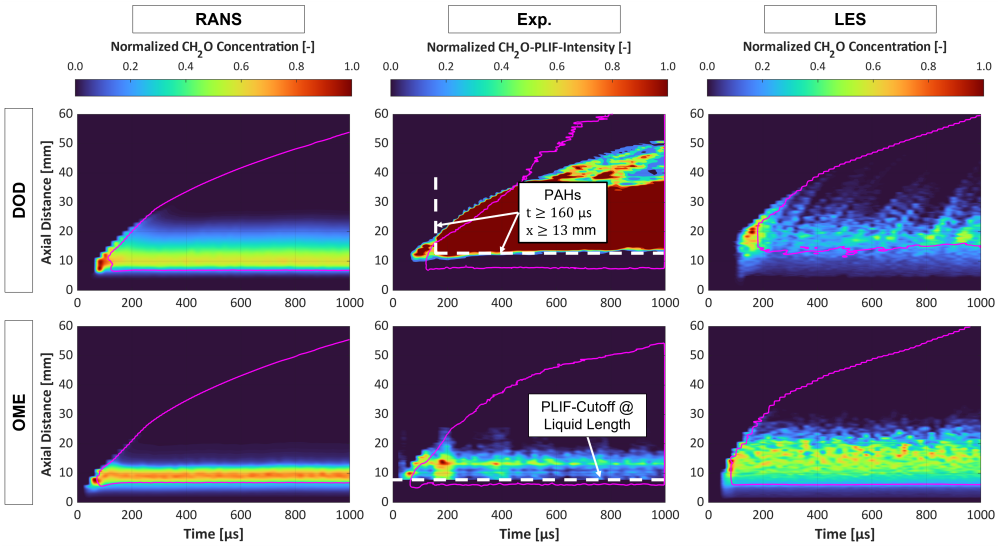

(**b**) OP2: 1200 K

Figure 4. Ensemble-averaged I_{xt} plot of CH_2O PLIF intensity (experiment) and molar concentration (simulations) in a slice cutting through the injector center. The magenta iso-lines indicate the line-of-sight OH^* and simulated projected OH molar concentration at the flame lift-off length.

After analyzing the global combustion behavior for both fuels and operating points, the spatial distribution of the high-temperature flame morphology will be discussed in detail. The results in Figures 5 and 6 are line-of-sight with the LES and RANS results showing projected OH species mass fractions.

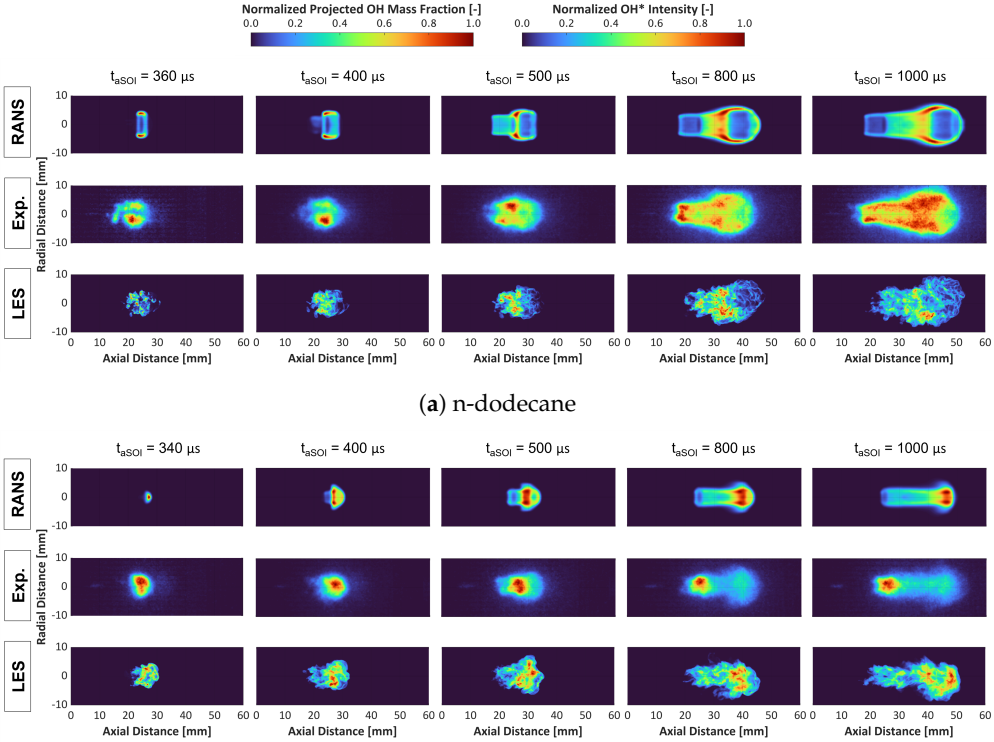

(**a**) n-dodecane

(**b**) OME

Figure 5. Time evolution of projected *OH* species mass fraction distribution for simulations and line-of-sight *OH** chemiluminescence intensity for experiments at 900 K ambient temperature (OP1).

The comparison between the two fuels for OP1 (900 K) in Figure 5 demonstrates significant differences in the spatial distribution of the high-temperature reaction zone, already observed in [17,18]. For n-dodecane (Figure 5a), the highest intensity is measured and simulated in the shear layer of spray and ambient air, which are also the locations of the first ignition kernels. As the flame propagates downstream, the high-intensity region stretches with it along the length of the spray. For OME (Figure 5b), the kernel of the ignition is at the tip of the spray in the center of the symmetry plane. The fuel-rich center of the spray remains the high-intensity region for the entire high-temperature combustion. Both simulations differ from the experiments in that the simulated peak of the *OH* species concentration travels with the flame downstream of the lift-off length. The experimentally observed peak of the excited *OH** radical maintains its position near the flame lift-off length. The overall contour is well represented by both simulations, with the LES being able to reproduce the high intensity in the spray center better than the RANS calculations.

The observation for the 1200 K operating point (OP2) in Figure 6 differs substantially from the 900 K case for OME. Now, the measured peak intensity location travels downstream in line with the simulation results instead of maintaining a high intensity near the lift-off length. Whereas the n-dodecane flame shape is similar to the 900 K case in forming high concentrations of *OH**/*OH* in the shear boundary layer between spray and ambient air, the analysis for OME shows that only its tendency to form high *OH**/*OH* concentrations in the spray center axis is also visible in the 1200 K case. The difference in the axial position of the peak intensity for OME when increasing the ambient temperature might be due to the decreased mixing time before high-temperature ignition. At 1200 K, the shortened ignition delay might cause fewer oxygen radicals to be present close to the flame lift-off length, which would generate a lower relative *OH** concentration.

The simulations' overall development and flame contour agree well with the experiments. The RANS calculations especially accurately replicate the radial and axial locations of the high intensity in the *OH** chemiluminescence experiments.

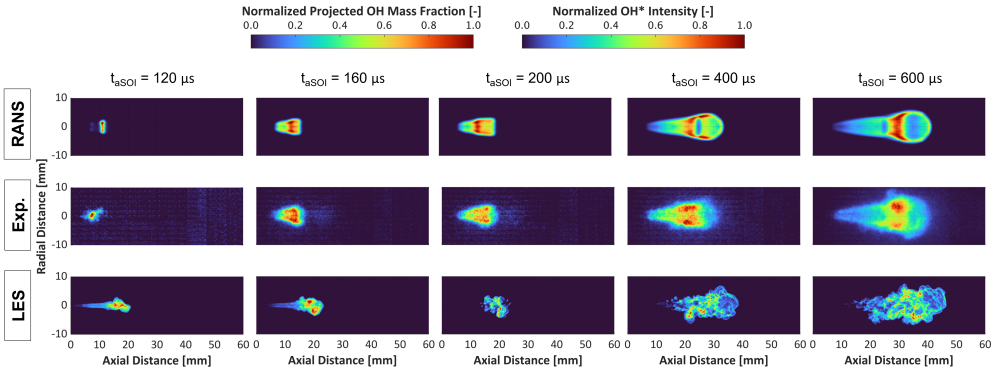

(**a**) n-dodecane

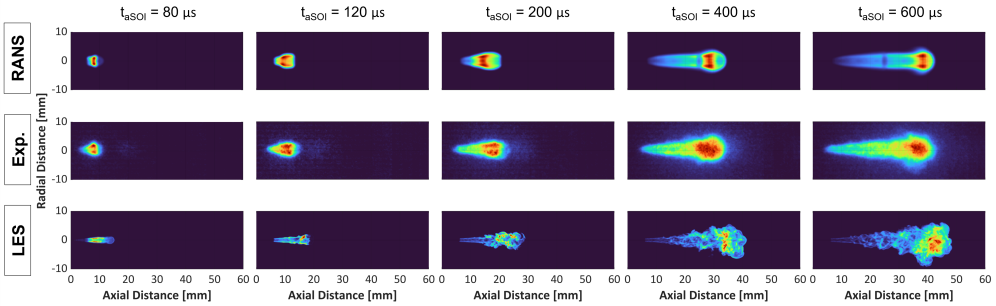

(**b**) OME

Figure 6. Time evolution of projected *OH* species mass fraction distribution for simulations and line-of-sight *OH** chemiluminescence intensity for experiments at 1200 K ambient temperature (OP2).

The experiments and simulations were averaged in time using the identical time window once a stable lift-off length was established for a more meaningful comparison of the low- and high-temperature species distribution. To analyze the high-temperature zones, the experimentally recorded *OH** line-of-sight data were deconvoluted using an inverse Radon transform to represent their distribution in the symmetry plane for the quasi-steady period. Table 5 shows the different averaging windows by fuel and operating point. In Figure 4, the quasi-steady period for the flame lift-off starting at approximately $t_{aSOI} > 500$ µs for each case indicates the timing for averaging the results for both fuels after establishing a stable flame lift-off.

As all contour plots were normalized by their respective maximum value for a better comparison between RANS and LES, the maximum simulated values for the concentrations of CH_2O and OH in the injector symmetry plane are listed in Table 6.

The influence of the ambient temperature on the time-averaged results for both fuels will be discussed in the following.

Figure 7 delivers a comprehensive comparison between simulations and experiments, n-dodecane and OME, as well as low- and high-temperature combustion for OP1 at 900 K ambient temperature. The contour plots show mean and normalized values, which were temporally averaged according to Table 5. At the top, Figure 7a displays the mean contour of the low-temperature steady-state combustion characterized by the distribution of formaldehyde in the spray symmetry plane. As indicated in the figure, the PLIF intensity for n-dodecane was only evaluated until an axial position of 30 mm downstream of the nozzle. Increased formation of PAHs was only detected for distances further downstream than that for 900 K ambient temperature, as seen in Figure 4a.

Table 5. Averaging periods for different experimental techniques and fuels.

Experiment	Temperature [K]	DOD Averaging Window [ms]	OME Averaging Window [ms]
*OH** Chemiluminescence	900	0.8–1.6	0.6–1.5
	1200	0.8–1.5	0.6–1.6
CH_2O PLIF	900	0.8–1.6	0.6–1.5
	1200	0.8–1.5	0.6–1.6

Table 6. Maximum simulated concentrations in symmetry plane.

Simulation	Temperature [K]	Max. CH_2O Concentration [mol/L]	Max. OH Concentration [mol/L]
RANS-DOD	900	1.37×10^{-2}	2.05×10^{-3}
RANS-OME		1.72×10^{-2}	1.65×10^{-3}
LES-DOD		2.18×10^{-2}	8.29×10^{-4}
LES-OME		2.56×10^{-2}	9.90×10^{-4}
RANS-DOD	1200	2.53×10^{-2}	2.62×10^{-3}
RANS-OME		3.29×10^{-2}	2.51×10^{-3}
LES-DOD		2.09×10^{-2}	1.36×10^{-3}
LES-OME		3.04×10^{-2}	2.34×10^{-3}

The peak in PLIF intensity and simulated CH_2O concentration can be located at approximately 20 mm in the center of the spray for both fuels. OME tends to concentrate its CH_2O formation a few millimeters further downstream. For the simulations, the zone of high-temperature combustion is shown with magenta iso-lines indicating a temperature of 1600 K, which, according to Idicheria and Pickett [46], serves as the best reference for marking the threshold of the destruction of CH_2O and the regime of high-temperature (OH^*) reactions. This observation is confirmed when analyzing Figure 7a, and later on in Figure 13 within Section 3.2, as for both fuels no significant amount of CH_2O enters the high-temperature zone. Additionally, fuel-rich regions in Figure 7 satisfying the criterion of $\phi = 2$ are shown with white iso-lines. Hereby, the equivalence ratio (ϕ) is defined as a passive scalar independent of the reaction state. For oxygenated fuels, such as OME, this definition has to be adapted by the chemically bound oxygen within the fuel structure following the conclusions of Mueller [47]. The existence of chemically bound oxygen causes the traditional definition of the equivalence ratio (ϕ) to incorrectly calculate the distance of a reactant mixture from its stoichiometric condition. Hence, the appropriate passive scalar mixing parameter for oxygenated fuels is the *oxygen equivalence ratio* (ϕ_Ω).

The differences between the two fuels are apparent when comparing the simulations. n-Dodecane fuel-rich zones penetrate the high-temperature regions for RANS and LES. For OME, the peak CH_2O concentration forms a distinct frontier separating the fuel-rich zone from the high-temperature flame. The clear spatial separation of the cool flame (CH_2O formation) and high-temperature (OH) reactions for OME at 900 K ambient temperature was also observed by simultaneous PLIF planar measurements of CH_2O and OH in [20] for an older generation of the Spray A injector.

When observing the high-temperature combustion, Figure 7b, the center region into which the n-dodecane-rich mixture ($\phi = 2$) penetrates is characterized by low OH^* intensity for the experiment and even lower OH concentration for the simulations. The lean OME spray, with its separated cool and hot flame, shows a very different flame morphology in the spray center plane. In the experiments especially, the OH^* intensity peaks only a few millimeters downstream of the lift-off length and remains elevated at the spray axis. Neither simulation can fully reproduce the stark contrast to n-dodecane in the high-temperature flame morphology. Notably, the simulations do not show the high-intensity blob shortly after the flame lift-off. The LES seems to be more capable in that regard, as it yields a higher OH concentration along the spray axis compared to RANS calculations.

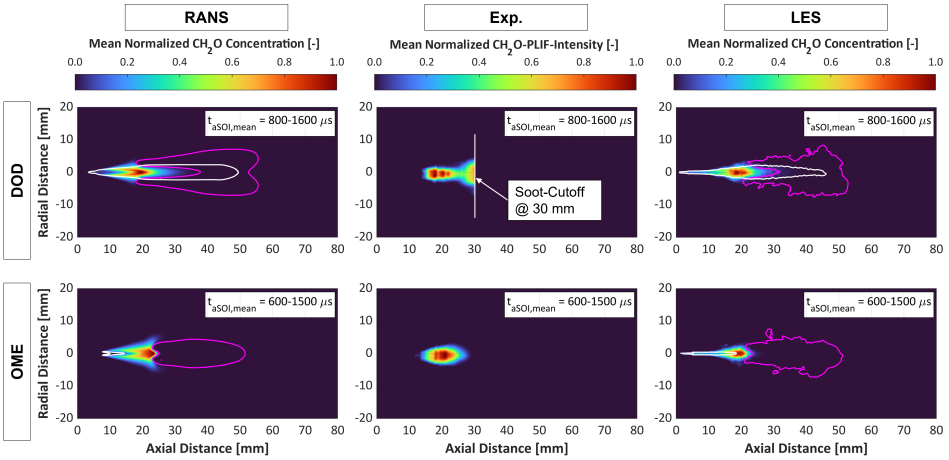

(**a**) Mean formaldehyde (CH_2O) distribution.

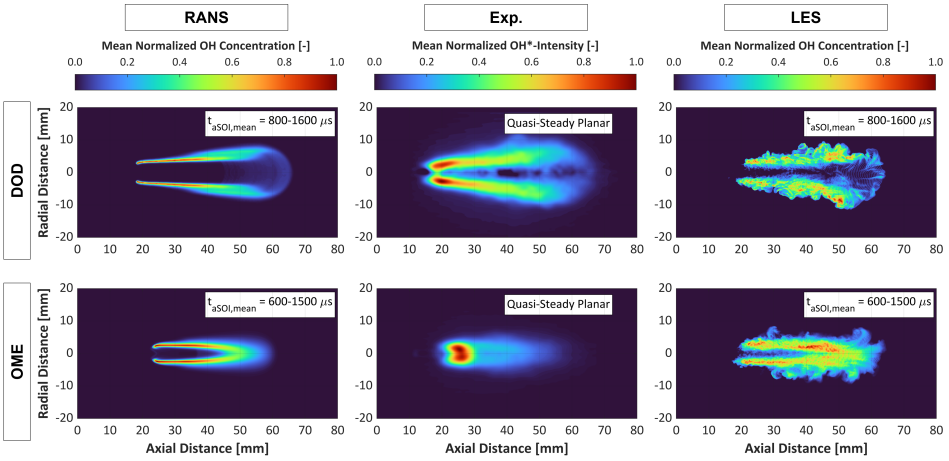

(**b**) Mean hydroxyl (OH^*/OH) distribution.

Figure 7. Time-averaged planar distribution of simulated OH (**bottom**) and CH_2O (**top**) concentration and experimental intensity for ambient conditions of 900 K and 15% oxygen content (OP1) in the spray symmetry plane.

It must be pointed out that differences are expected when comparing simulated *OH* concentration to measured *OH** chemiluminescence intensity. Maes et al. [48] investigated the flame structure differences of excited *OH** chemiluminescence and ground state *OH* PLIF. The flame structure differed depending on the measurement technique, with *OH** found further upstream than *OH* and the latter extending to a greater radial distance from the spray centerline. It was concluded that *OH* is more stable and in partial equilibrium with the water vapor produced during combustion. *OH**, on the other hand, is instead a reaction zone product for which spontaneous emission rates determine the lifetime.

These observations explain the discrepancies between experiment and simulations, seen in Figure 7b, to some extent, but not sufficiently. The differences between simulations and experiments concerning the high-temperature flame shape seem significantly greater for OME than for n-dodecane. Even the computationally expensive LES calculations cannot fully capture the flame morphology of OME reliably for the presented ambient conditions of 900 K.

The interpretation of the differences between simulations and experiments and between n-dodecane and OME slightly changes when studying the time-averaged contour maps with 1200 K ambient temperature in Figure 8. As seen with the transient *OH**/*OH* plots for OME in Figure 6b, the time-averaged experimental results at 1200 K in Figure 8b show an entirely different *OH** distribution compared to its 900 K counterpart. The peak

intensity is close to the flame lift-off length and the spray tip. The spray center axis displays an elevated OH^* concentration. Still, high levels are also seen a few millimeters away from the centerline in what appears to be the boundary shear layer of OME fuel spray and ambient air. Interestingly, n-dodecane also shows some differences at 1200 K in its high-temperature flame shape. The peak of its mean distribution is now further upstream along the shear boundary of spray and air and not near the lift-off length as seen in Figure 7b at 900 K ambient temperature. The 1200 K simulations match the experiments more accurately than in the 900 K case, especially for OME.

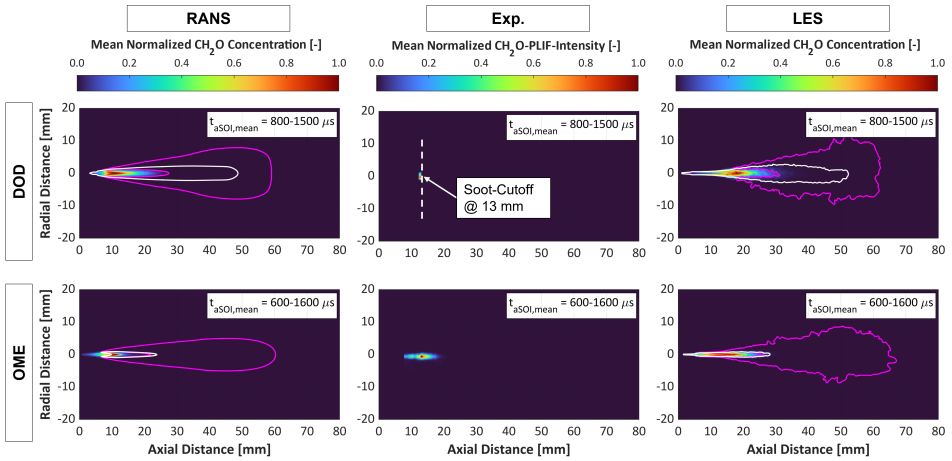

(**a**) Mean formaldehyde (CH_2O) distribution.

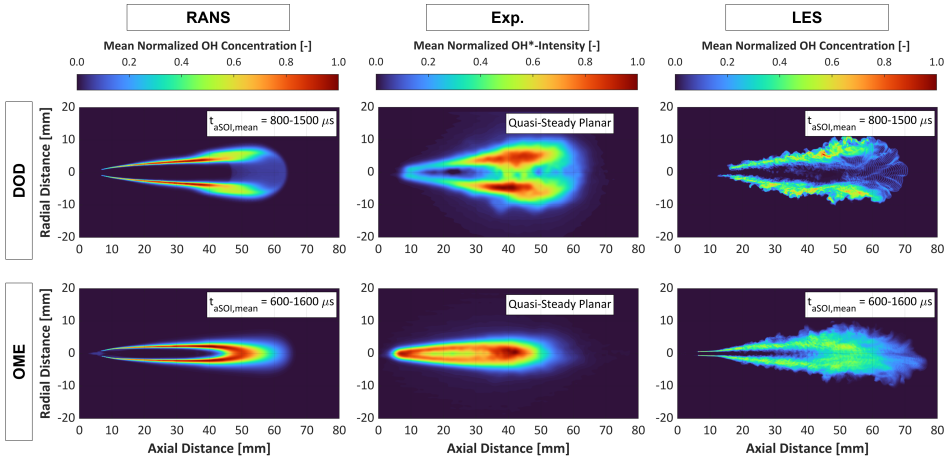

(**b**) Mean hydroxyl (OH^*/OH) distribution.

Figure 8. Time-averaged distribution of simulated OH (**bottom**) and CH_2O (**top**) concentration and experimental intensity for ambient conditions of 1200 K and 15 % oxygen content (OP2).

The results for the mean cool-flame shape are displayed in Figure 8a. As is indicated in the I_{xt} plots of Figure 4b, the PLIF measurements for n-dodecane are impaired by the presence of PAHs, which are entirely absent for OME. The soot cutoff axial position shown in Figure 8a virtually denies an adequate assessment of the time-averaged cool-flame distribution for n-dodecane. When comparing RANS and LES at 1200 K for n-dodecane, it is noticeable that the LES predicts an CH_2O distribution that penetrates further into the combustion chamber compared to RANS, which also pushes the high-temperature zone (magenta iso-line) further downstream. The same observation is made for OME. Here, because of the absence of PAH concentration, it is discernable that the RANS calculation delivers results closer to predicting the measurements.

The clear axial separation of the cool and hot OME spray flame is not present at 1200 K. Fuel-rich spray ($\phi = 2$, white iso-lines) penetrates along the centerline and forms CH_2O

with the high-temperature zone already present in short radial distance to it. However, the fuel-rich spray enters the area of $T \geq 1600$ K only very marginally, especially compared to n-dodecane.

For a more detailed analysis of the spatial high-temperature flame distribution, radial profiles are drawn at axial positions, starting a few millimeters downstream of the lift-off length, into the time-averaged contours. Figure 9 shows the normalized *OH* and *OH** profiles for simulations and experiments at 900 K ambient temperature, respectively. The differences between n-dodecane and OME become visible once again, with OME not displaying any drop in its *OH** intensity at the center of the spray.

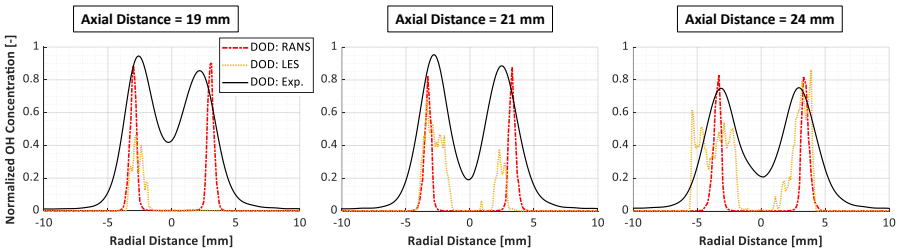

(**a**) n-dodecane

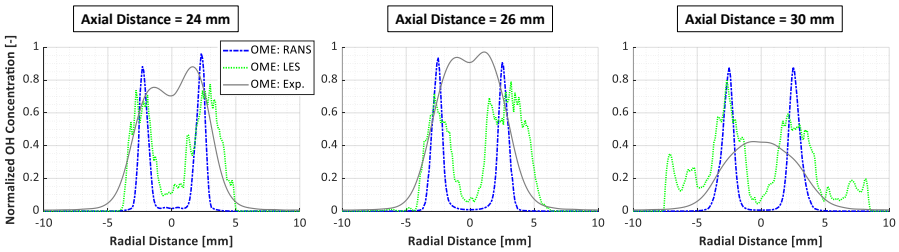

(**b**) OME

Figure 9. OH radial profiles for time-averaged contours at different axial positions at 900 K ambient temperature (OP1).

The simulations are able to predict the peak intensity location for n-dodecane with good agreement to the experiments, with the LES showing a radially wider distribution of high *OH* concentration peaks stretching further away from the shear layer of fuel and ambient air. For n-dodecane, a reduction in the *OH** intensity in the center is measured, which falls to approximately 20% of its peak intensity 24 mm downstream of the nozzle and several millimeters downstream of the lift-off length. The fact that the *OH** profile does not entirely subside to zero in the center for the experiments with n-dodecane cannot be reproduced by either simulation.

This behavior is even more pronounced for OME, where the respective experimentally observed peak intensity is right in the center axis of the spray. The RANS simulations again show sharp concentration peaks roughly one millimeter closer to the center axis than the respective RANS n-dodecane calculation. The LES shows slightly more evenly distributed profiles, which have an elevated *OH* concentration in the center, albeit not enough to align with the experiments.

When considering the 1200 K operating point in Figure 10, it can be seen that for n-dodecane, the *OH** intensity does not drop at all the further downstream the radial profiles are extracted (Figure 10a). It instead increases, which is reflected by the LES calculation. The peak intensity can be found at $x = 40$ mm, with both simulations predicting the radial position of the peak intensity correctly. The RANS calculation cannot replicate the increase in *OH* concentration and only shows a widening of the radial profiles. Both simulations cannot reproduce the level of *OH** intensity in the spray center, similar to the 900 K ambient conditions.

The radial profiles for OME at 1200 K, Figure 10b, show a distinct difference from their 900 K counterparts. A few millimeters downstream of the lift-off length, the typical peak OH^* intensity in the spray center axis is measured. However, further downstream at $x = 20$ mm, a drop in intensity in the spray center is visible, producing a similar radial profile shape compared to n-dodecane, with higher relative values for OH^* intensity. At the flame tip, the intensity peaks again at the center, which the simulations can partly capture, showing elevated OH concentrations on the spray center axis at $x = 45$ mm downstream of the nozzle.

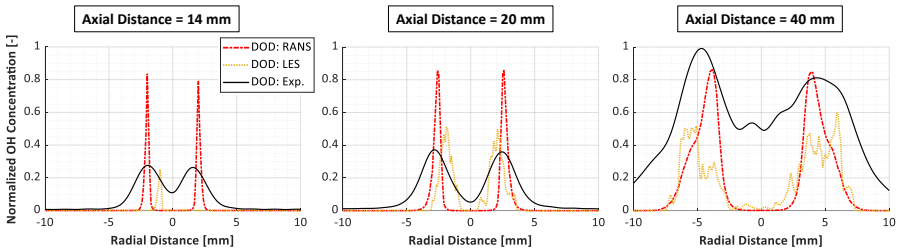

(**a**) n-dodecane

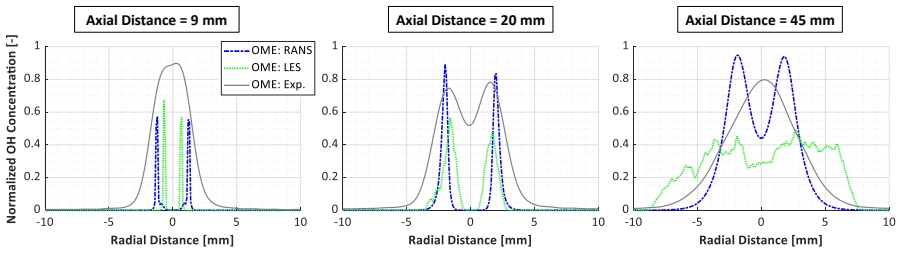

(**b**) OME

Figure 10. OH radial profiles for time-averaged contours at different axial positions at 1200 K ambient temperature (OP2).

The following analysis aims at depicting the spatial transition of cool (CH_2O) to hot flame OH^*/OH for the two studied ambient temperatures and fuels with Figure 11, where the transition from cool- to high-temperature flame along the spray centerline is depicted for the time-averaged results of the measurements and simulations.

At 900 K, OME decreases its OH^* intensity level faster than n-dodecane the greater the distance downstream of the lift-off length. This sharp drop in high-temperature reaction activity can also be noticed in Figure 11b. In contrast to n-dodecane, Figure 11a, the maximum OH^* intensity for OME drops from approximately 90% to below 25% within only 5 mm along the centerline.

Another important aspect is the location of the first rise of OH^* intensity compared to the location of maximum CH_2O formation. For n-dodecane at 900 K, the measured peak OH^* intensity in Figure 11a falls precisely within the space of elevated and peak CH_2O PLIF intensity. The simulations capture the formation and conversion of CH_2O in the center of the spray very well. However, the transition to OH is less accurate due to the already shown lack of simulated OH species concentration in the spray center.

In the case of OME fuel, a clear shift of the maximum OH^* intensity further downstream relative to the maximum CH_2O PLIF intensity is visible in Figure 11b. The peak of OH^* intensity now occurs at an axial location of approximately 26 mm where all CH_2O is already destroyed, leading to a clear separation of the cool flame and the zone of high-temperature combustion. The RANS calculations slightly overestimate the axial distance of maximum CH_2O formation, which the LES predicted with higher accuracy. The underestimation of the OH reaction activity in the spray center is also responsible for the late rise in OH concentration in both simulations.

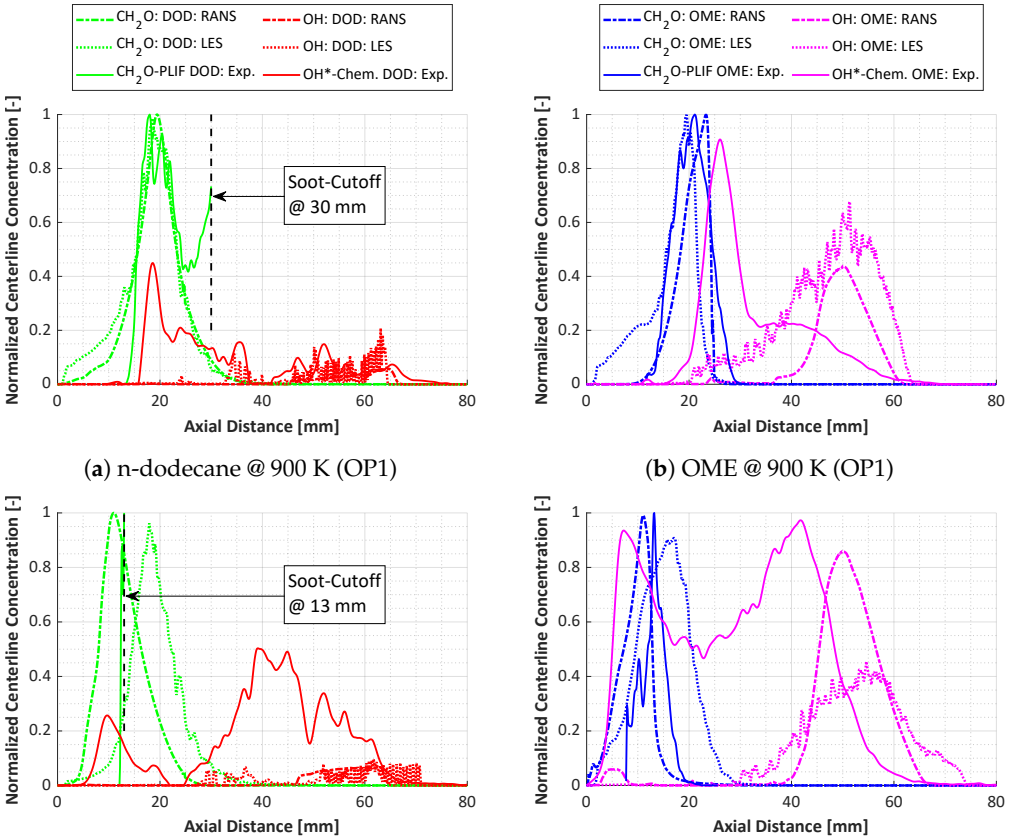

(**a**) n-dodecane @ 900 K (OP1) (**b**) OME @ 900 K (OP1)

(**c**) n-dodecane @ 1200 K (OP2) (**d**) OME @ 1200 K (OP2)

Figure 11. CH_2O and OH profiles at the center axis of spray for time-averaged contours.

By increasing the combustion chamber temperature to 1200 K, the OH^* chemiluminescence experiments show two peaks in intensity for both fuels, one close to the lift-off length and one further downstream. For n-dodecane, Figure 11c, the first peak of OH^* intensity at approximately $x = 9$ mm occurs even before any CH_2O PLIF signal is detected. The same observation is valid for OME in Figure 11d, with the maximum of OH^* intensity appearing before the maximum of CH_2O, and the second one at the end of the flame at approximately $x = 42$ mm. However, it must be noted that the PLIF measurements cannot detect any signal where liquid fuel is present. Hence, the axial location of CH_2O maximum PLIF intensity cannot be determined with certainty for both fuels in 1200 K hot ambient temperature. For OME, though, the centerline profile strongly suggests that the maximum of CH_2O intensity does not form upstream of the PLIF starting threshold of $x = 8$ mm. For n-dodecane, between soot cutoff and PLIF threshold, the first rise and onset of CH_2O are very challenging to discern, with only a few millimeters of actual CH_2O signal detectable.

The LES at 1200 K pushes its CH_2O maximum further downstream compared to RANS, and there seems to be a smooth transition from consumed CH_2O to forming of OH, especially for OME. The RANS calculation for OME in Figure 11d shows a slight increase in OH concentration at the exact location of the first axially measured OH^* intensity peak. It also predicts a comparable, and higher in comparison to the 900 K case, level of OH concentration only slightly downstream of the second OH^* intensity peak. The LES cannot replicate the changed hot-flame morphology for this case and shows a similar profile compared to 900 K ambient temperature.

In general, RANS and LES struggle to reproduce the high level of high-temperature reactions in the spray center close to the lift-off length of the flame for both fuels and ambient temperatures, especially for OME.

3.2. Cool-Flame Evolution

Tagliante et al. identified in [24] several distinct stages for the combustion of n-dodecane using the same injector at 900 K ambient temperature to characterize the transition from cool flame to high-temperature combustion. Figure 12 displays the different ignition stages using the spatially averaged but transient profiles of planar formaldehyde (CH_2O) and line-of-sight OH^*/OH for n-dodecane (Figure 12a) and OME (Figure 12b) at 900 K ambient temperature. Because of the rapidness of the combustion process, the PLIF signal axial thresholds and early formation of PAHs in case of 1200 K, see Figure 4b, the cool-flame transient development and subsequent combustion stages will be discussed in detail for the 900 K case only.

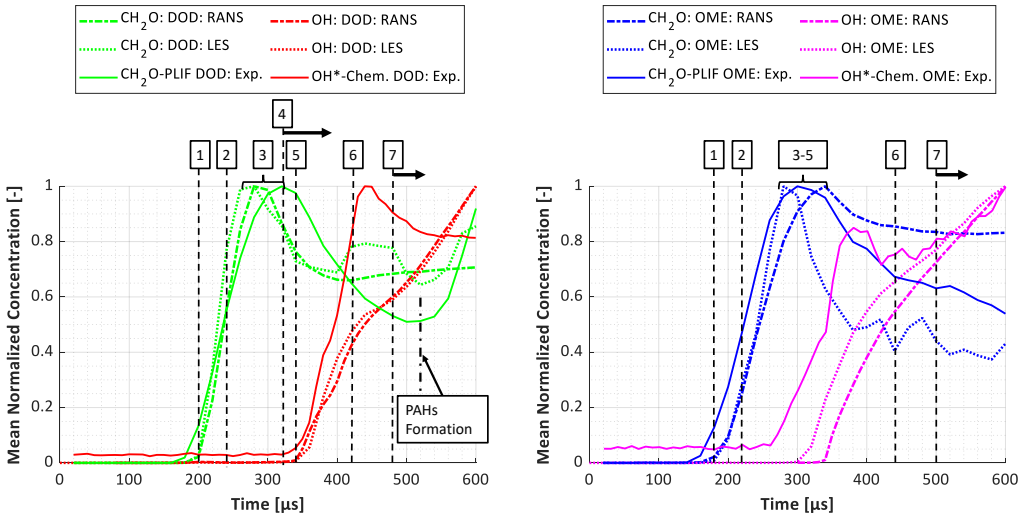

(**a**) n-dodecane (**b**) OME

Figure 12. Time- resolved and spatially averaged evolution of planar CH_2O and line-of-sight OH/OH^* profiles with indicated combustion stages at 900 K ambient temperature (OP1).

In general, seven stages can be distinguished in Figure 12: (1) first stage of ignition, (2) cool flame (low-temperature) propagation, (3) maximum CH_2O, (4) CH_2O consumption, (5) second stage ignition, (6) turbulent high-temperature flame propagation, and (7) quasi-steady combustion. Depending on the fuel characteristics and ambient conditions, these stages occur at different time intervals, which may overlap. For n-dodecane in Figure 12a, it is indicated that stages are quite distinct from each other when considering that the ignition delay, signaling the combustion stage (5), of the simulations is $ID_{DOD,RANS,LES} = 340$ µs and that of the experiments ranges from $ID_{DOD,EXP} = 331 - 368$ µs.

For OME in Figure 12b, the analysis is more complex, as the measured ignition delay time ranges from $ID_{OME,EXP} = 309 - 340$ µs. The LESs predict an ID of $ID_{OME,LES} = 270$ µs, whereas the RANS calculations pinpoint the largest temperature gradient at $ID_{OME,RANS} = 327$ µs. It is therefore challenging to differentiate between the stages (3), (4), and (5) for OME in simulations and experiments, as the second stage ignition, i.e., ignition delay, occurs almost simultaneously with the maximum yield of CH_2O and its subsequent consumption. OME tends to pass through the initial stages of combustion earlier than n-dodecane, with both simulations somewhat overpredicting the delay of the first ignition stage for both fuels. The LES shows a steeper accumulation curve of CH_2O compared to RANS, which is more pronounced for OME. The consumption of CH_2O (stage 4) in the case of n-dodecane is quite similar for LES and RANS and only shifted compared to the measurements. For OME, this combustion stage deviates significantly for LES and RANS, leading to a difference in ignition delay prediction of more than 50 µs. The consumption of the CH_2O concentration after its maximum was reached is more rapid for the LES and seems too fast compared to the experiment.

The quasi-steady combustion for n-dodecane is characterized by increased measured PLIF intensity after $t_{aSOI} > 520$ µs. This uptake is due to the formation of PAHs.

The spatial distribution of the temporal development of the cool flame and the onset of the high-temperature reactions, referring to the combustion stages shown in Figure 12, are depicted in Figure 13 for the 900 K ambient temperature (OP1). The planar contour plots show the PLIF intensity for the experiment and molar concentration for the simulations. The intensity and concentration were normalized to accurately compare each time step. For the simulations, the fuel-rich ($\phi = 2$) and high-temperature reaction ($T = 1600$ K) zones are again outlined in white and magenta iso-lines, respectively.

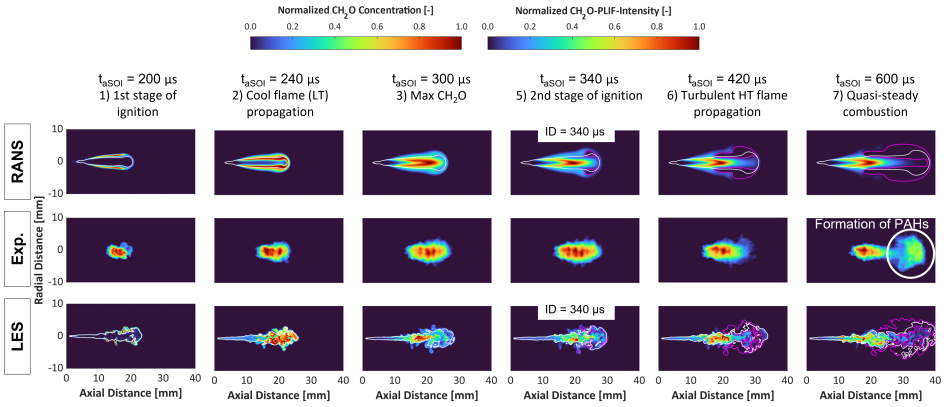

(**a**) n-dodecane

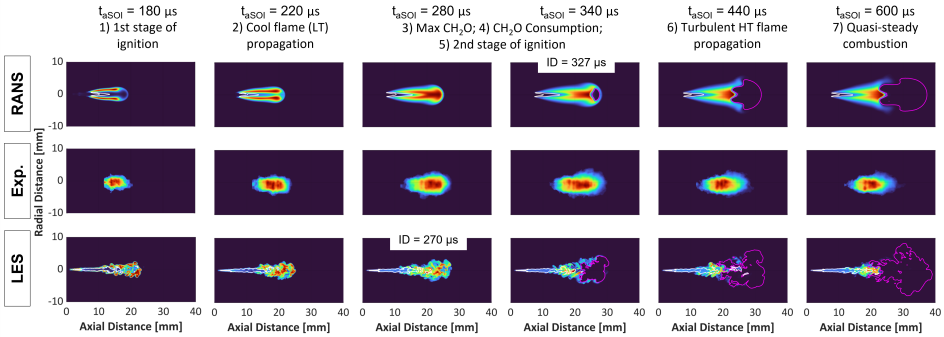

(**b**) OME

Figure 13. Time evolution of CH_2O concentration distribution for simulations and PLIF intensity for experiments in the symmetry plane at 900 K ambient temperature (OP1). The high-temperature zones with $T > 1600$ K are indicated with magenta iso-lines. Fuel-rich regions ($\phi = 2$) are shown with white iso-lines.

In Figure 13a, n-dodecane is simulated by the RANS and LES methods to penetrate with a fuel-rich spray into the high-temperature zone. The first low-temperature ignition kernels (first stage) can be seen at the shear layer of the fuel spray with ambient air, which differs from the experiments, where the initial CH_2O formation appears in the spray center. The simulations correctly predict the location of maximum CH_2O (third stage) in the spray center. The first spots of high-temperature ignition (fifth stage) for n-dodecane are simulated at the spray tip but again in the shear layer between fuel spray and ambient air. At $t_{aSOI} = 600$ µs, during the quasi-steady combustion, it is noticeable that the PLIF experiments start to show elevated concentrations of PAHs at the spray tip precisely at the locations where the RANS and LES methods predict the fuel-rich mixture to enter the high-temperature region. In contrast, Figure 13b visualizes the absence of any fuel-rich spray entering the simulated spray region with $T > 1600$ K for OME. The simulations predict a clear spatial separation of the cool flame (CH_2O formation) and high-temperature

(*OH*) reactions for every time step, as was already observed for the time-averaged plots in Figure 7a.

The first ignition stage appears more accurate for OME simulations, with CH_2O forming closer to the spray center axis. The LES represents both fuels' cool-flame propagation (second stage) well. Both simulations can capture the position of maximum CH_2O. In contrast to n-dodecane, high-temperature ignition locations for OME are spotted at the spray tip instead of at the shear layer between the spray and ambient air.

In general, the locations of CH_2O formation are well captured by LES and RANS calculations, with the experimental intensity and simulated concentration for both fuels peaking at approximately 20 mm downstream of the nozzle.

The last aspect of the present study concerns the initial cool-flame propagation of accumulated CH_2O mass within the mixing space, as well as its periodic formation and destruction during the quasi-steady combustion. Figures 14 and 15 show the simulated CH_2O and *OH* mass binned by equivalence ratios (ϕ) from 0 to 10 for n-dodecane and OME, respectively, for both turbulence models, with a bin size of 0.05. The symbols show the average mass of CH_2O (left *y*-axis) and *OH* (right *y*-axis) in each bin, color-coded by temperature. The shaded areas represent the standard deviations, with CH_2O in blue and *OH* in red. The top plots focus on the cool-flame formation and consumption before high-temperature ignition for each fuel and simulation model. The bottom plots show CH_2O and *OH* during quasi-steady combustion.

Tagliante et al. [24] demonstrated an initial *cool-flame wave*, identified by CH_2O and defined in [49], for n-dodecane and LES, as well as its periodic formation/consumption during the quasi-steady phase. This study also calculated this process and it is shown in Figure 14b. The comparison between LES and RANS for n-dodecane and 900 K is particularly interesting as both simulations predict the exact same high-temperature ignition delay of 340 µs; see Figure 3a. The RANS calculations with n-dodecane in Figure 14a also visualize a cool-flame wave, albeit at leaner mixtures and slightly lower temperatures. At 240 µs CH_2O peaks at $\phi = 4.3$ and *OH* at $\phi = 5$ for the LES. For this time step, the RANS model, on the other hand, simulates a peak CH_2O concentration for $\phi = 2.6$. Corresponding to the trend for the LES, the maximum *OH* accumulated mass is found for a slightly richer mixture at $\phi = 2.8$. 40 µs later in the injection process, the LES predicts that the cool flame propagated to leaner mixtures peaking at $\phi = 7$ and starts being consumed at $\phi = 2$. At this point in time, the RANS model simulates the CH_2O mass to peak already at $\phi = 4$. The high-temperature consumption forming *OH* shows two maxima at $\phi = 4.4$ and $\phi = 2.8$, with the leaner value being the mixing region of increased *OH* production, ultimately peaking at stoichiometry. The entire process of the initial cool-flame propagation is limited in temperature for the LES by $T \leq 1400$ K and for RANS by $T \leq 1200$ K.

Within the LES framework, the quasi-steady combustion period for n-dodecane is characterized by the cyclic formation and consumption of CH_2O, as shown at the bottom in Figure 14b. According to [24], this process is most likely caused by gas pressure oscillations generated by the low-temperature combustion. The oscillation frequency qualitatively matched the resonance frequency of the combustion chamber (5.7 kHz) because the length of LES mesh matched the length of the pre-burn chamber. The LES can capture these fluctuations affecting the CH_2O distribution at the jet center, potentially because of its well-resolved turbulent mixing field, which is fine enough to resolve at least 80% of the turbulent kinetic energy. The RANS calculations, however, are not able to resolve these small-scale fluctuations. The turbulent mixing field is too smooth to reproduce the oscillations. No cyclic behavior in the formation and consumption of CH_2O during quasi-steady combustion, at the bottom in Figure 14a, could be observed for the RANS computations.

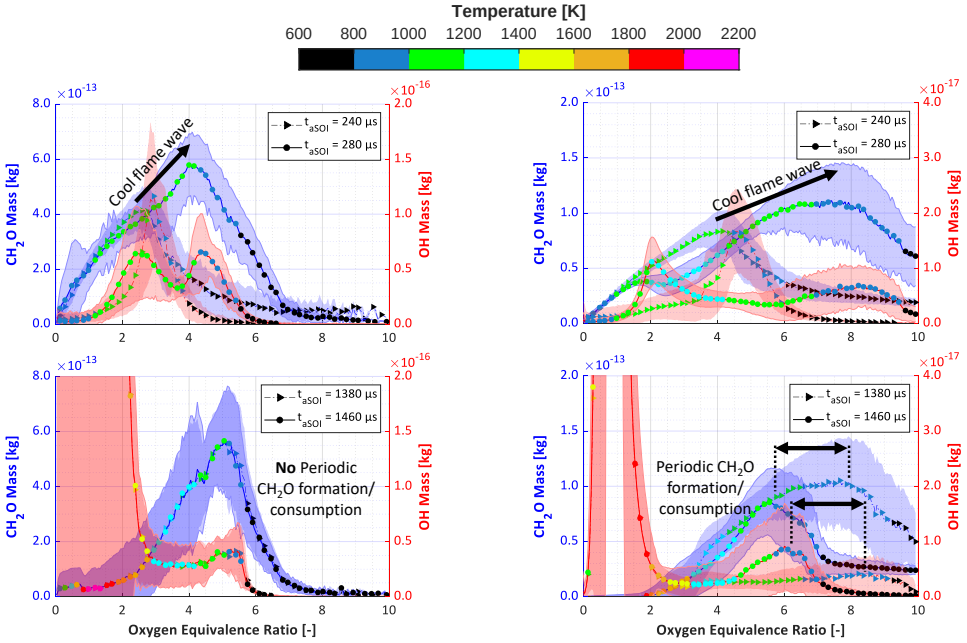

(**a**) RANS: n-dodecane (**b**) LES: n-dodecane

Figure 14. CH_2O and OH mass binned by equivalence ratio from 0 to 10 for n-dodecane fuel at 900 K ambient temperature (OP1) with a bin size of 0.05. The symbols show the average mass of CH_2O (left y-axis) and OH (right y-axis) in each bin sample, colored with its average temperature.

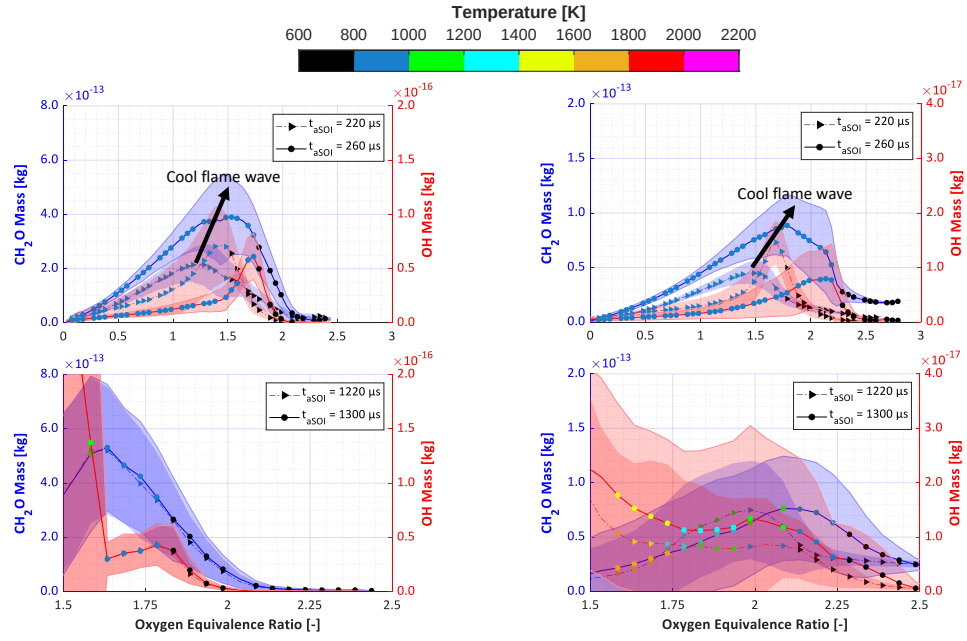

(**a**) RANS: OME (**b**) LES: OME

Figure 15. CH_2O and OH mass binned by equivalence ratio from 0 to 10 for OME fuel at 900 K ambient temperature (OP1) with a bin size of 0.05. The symbols show the average mass of CH_2O (left y-axis) and OH (right y-axis) in each bin sample, colored with its average temperature.

For OME, both LES (Figure 15b) and also RANS (Figure 15a) depict the cool-flame propagation from lean to rich mixtures after the first stage of ignition. In this case, however, the propagation ends at mixtures with $\phi < 3$ and for RANS even $\phi < 2.5$. LES and RANS show a similar initial process, only shifting to smaller equivalence ratio values by 0.3–0.5. Interestingly, the average temperature for each bin does not exceed 1000 K for both

simulations during the cool-flame propagation and is, therefore, significantly cooler than its counterpart for n-dodecane.

Concerning the quasi-steady combustion, it is quite challenging to discern cyclic behavior for OME, even when analyzing LES calculations. The bottom plot in Figure 15b hints at a possible periodic behavior. However, the small range of equivalence ratios in which the entire combustion process occurs complicates the identification of cycles. The RANS calculations, again, show a complete absence of periodic behavior, as the averaging process of the simulations makes it impossible to capture the small-scale oscillations caused by the low-temperature flame forming and consuming CH_2O and transmitted by acoustic pressure waves in the combustion chamber.

4. Summary and Conclusions

This study focused on the influence of high ambient temperature on the cool- and hot-flame morphology, represented by CH_2O and OH^*/OH, for the synthetic e-fuel OME_{3-5} compared to the diesel-like reference fuel n-dodecane. Besides the standard and well-documented ECN Spray A operating point of 900 K, the spray combustion of the two fuels in an ambient temperature of 1200 K was analyzed with PLIF CH_2O and OH^* chemiluminescence experiments, as well as RANS and LES calculations. In addition, the initial cool-flame wave and the periodic formation and consumption during the quasi-steady combustion regime were compared for the two fuels and turbulence modeling methods. The following conclusions were drawn:

- OME forms no visible PAHs or soot signature within the CH_2O PLIF experiments at neither 900 K nor 1200 K. This contrasts with n-dodecane, which shows PAH formation at both temperatures. In the case of 1200 K and n-dodecane, the early onset of PAHs generation after high-temperature ignition and its proximity to the injector nozzle makes it very challenging to differentiate between actual CH_2O signal detection and PAH interference.
- At 900 K, OME shows a distinct separation between the fuel-rich ($\phi = 2$) spray, the cool-flame distribution signaled by CH_2O, and the high-temperature region ($T \geq 1600$ K) of the spray. No fuel-rich spray enters the high-temperature zone, either for LES or RANS. At 1200 K, this clear axial separation does not exist. However, little fuel-rich spray enters the simulated zone with $T \geq 1600$ K. For n-dodecane, the fuel-rich spray is simulated to penetrate the hot-flame region, and PAH formation is experimentally detected at identical locations.
- The spatial cool-flame (CH_2O) distribution and its temporal evolution are predicted by both turbulence modeling techniques with good agreement to the experiments.
- The high-temperature flame distribution shows significant differences between fuels and ambient temperatures. At 900 K, the simulations fail to predict the high OH^* intensity close to the lift-off length, especially for OME, where the signal intensity at the spray tip is only a fraction of its maximum close to the root of the flame. This picture changes significantly for 1200 K, where the peak intensity for OME travels along the spray tip and two distinct OH^* maxima of intensity are detected, which is simulated by both LES and RANS with better agreement compared to the 900 K case. This difference in the axial location of the peak intensity for OME for an increased ambient temperature might be caused by the decreased mixing time before high-temperature ignition, with possibly fewer oxygen radicals present close to the flame lift-off length, generating a lower relative OH^* concentration.
- The LES calculations are better suited to reproduce the higher OH^* intensity for OME in the spray centerline and its radial distribution close to the lift-off length. However, especially for the lower ambient temperature of 900 K, the discrepancies between experimental OH^* and simulated OH species contours are significant. The deviations are less severe but still present for n-dodecane. This indicates a generic problem, which only intensifies for OME.

  An explanation might be that the studied reaction mechanism for OME developed by

Niu et al. [30] does not contain an equivalent excited OH^* species, which is assumed to be less stable with its lifetime limited by spontaneous emission rates and also appears to be present further upstream than the ground state OH species [48].
Another possibility, which refers to the differences seen for OME and n-dodecane, is that the current OME mechanism incorrectly models the impact of the chemically bound oxygen, or its release via fuel decomposition, on the high-temperature reactivity in the fuel-rich center of the spray.

- The overall high-temperature flame morphology at 1200 K is well captured by the RANS computations.
- The cool-flame wave of CH_2O formation within different mixing states for n-dodecane, previously shown in [24], was demonstrated for OME too. Both LES and RANS predict an increase in CH_2O mass after the first stage of ignition, which materializes initially at small equivalence ratio values and then propagates to reach its peak at fuel-rich mixtures. The LES predicts this process within a wider range of equivalence ratios. The most significant differences regarding this analysis are shown between the two fuels, with OME barely exceeding values for equivalence ratios of $\phi > 2.5$ and n-dodecane, especially for LES, showing accumulations of CH_2O with $\phi > 10$. Also, the initial cool-flame wave occurs at lower temperatures for OME ($T \leq 1000$ K) compared to n-dodecane ($T \leq 1400$ K).
- The periodic formation and consumption of formaldehyde described in [24] could not be reproduced with RANS calculations. In the case of LES with OME as fuel, oscillations for the formation and subsequent destruction of CH_2O in the mixing space are visible but occur within a very narrow range of equivalence ratios.

Future work in the area of this study should focus on the development of numerical reaction mechanisms for OME, which contain excited OH^* as well as ground state OH species, to be able to reference experiments that use either OH^* chemiluminescence or OH PLIF.

In addition, the influence of chemically bound oxygen in oxygenated fuels on high-temperature reactions needs further investigation. Currently, fuel-rich regions, like the center of a spray jet, are the primary source of modeling errors when dealing with oxygenated fuels like OME. Identifying the origin of the error, be it incorrect fuel decomposition or inadequate reaction rates of specific reactions, will be the main challenge to improving CFD modeling quality for OME fuel.

Author Contributions: Conceptualization, F.W.; methodology, F.W., T.M.N., F.T., L.M.P., J.M. and T.L.; software, F.W. and T.M.N.; validation, F.W., T.M.N. and J.M.; formal analysis, F.W.; investigation, F.W., T.M.N., F.T., K.W. and J.M.; data curation, F.W., T.M.N. and K.W.; writing—original draft preparation, F.W. and T.M.N.; writing—review and editing, T.L. and K.W.; visualization, F.W.; supervision, T.L., J.M. and L.M.P.; project administration, T.L.; funding acquisition, T.L. All authors have read and agreed to the published version of the manuscript.

Funding: The work at the TU Wien was funded by the *Federal Ministry of Climate Action, Environment, Energy, Mobility, Innovation and Technology* (BMK) through the *Austrian Research Promotion Agency* (FFG), grant number 874418. The research was carried out in the framework of the *collective research networking program* (CORNET) project "eSpray". The experiments performed at Sandia Nat. Labs were supported by the U.S. Department of Energy (DOE) Office of Vehicle Technologies. Sandia is a multi-mission laboratory managed and operated by National Technology and Engineering Solutions of Sandia, LLC., a wholly owned subsidiary of Honeywell International, Inc., for the U.S. Department of Energy's National Nuclear Security Administration under contract DE-NA000352.

Data Availability Statement: The raw data supporting the conclusions of this article will be made available by the authors on request.

Acknowledgments: The authors would like to thank TU Wien Bibliothek for financial support through its Open Access Funding Program. The authors gratefully acknowledge Convergent Science Inc. for their licensing and technical supports. The authors would like to thank Steven Luna for his support this research. The computational results presented in this study have been achieved using

the Vienna Scientific Cluster (VSC) via the funded project No. 71485 and the computational resources sponsored by the Department of Energy's Office of Energy Efficiency and Renewable Energy and located at the National Renewable Energy Laboratory.

Conflicts of Interest: The authors declare that they have no known competing financial interests or personal relationships that could have appeared to influence the work reported in this paper.

Abbreviations

The following abbreviations are used in this manuscript:

AMR	Adaptive Mesh Refinement
ASG	Analytik Service Gesellschaft
B_0,B_1	KH-RT breakup Model Parameters
ECN	Engine Combustion Network
f	Elliptic Relaxation Function in $k-\zeta-f$ Turbulence Model
ID	Ignition Delay
k	Turbulent Kinetic Energy
KH-RT	Kelvin–Helmholtz–Rayleigh–Taylor Breakup Model
LES	Large-Eddy Simulations
LLNL	Lawrence Livermore National Laboratory
LOL	Lift-Off Length
OME/PODE	Polyoxymethylene Dimethyl Ethers
OP1	ECN Spray A standard reacting chamber conditions (900 K, 22.8 kg/m^3, 15% O_2)
OP2	ECN Spray A high-temperature reacting chamber conditions (1200 K, 22.8 kg/m^3, 15% O_2)
p	Pressure
PAH	Polycyclic Aromatic Hydrocarbons
PLIF	Planar Laser-Induced Fluorescence
RANS	Reynolds Averaged Navier–Stokes Equations
SOC	Start of Combustion
SOI	Start of Injection
t	Time
$\overline{v^2}$	Velocity Scale (wall-normal)
x	Distance
ϵ	Turbulent Dissipation Rate
ζ	Velocity Scales Ratio
ρ	Density
ϕ	Equivalence Ratio
ϕ_Ω	Oxygen Equivalence Ratio
Ω	Oxygen Ratio

References

1. Burger, J.; Siegert, M.; Ströfer, E.; Hasse, H. Poly(oxymethylene) dimethyl ethers as components of tailored diesel fuel: Properties, synthesis and purification concepts. *Fuel* **2010**, *89*, 3315–3319. [CrossRef]
2. Pellegrini, L.; Marchionna, M.; Patrini, R.; Beatrice, C.; Del Giacomo, N.; Guido, C. *Combustion Behaviour and Emission Performance of Neat and Blended Polyoxymethylene Dimethyl Ethers in a Light-Duty Diesel Engine*; SAE Technical Paper 2012-01-1053; SAE: Warrendale, PA, USA, 2012. [CrossRef]
3. Härtl, M.; Gaukel, K.; Pélerin, D.; Wachtmeister, G. Oxymethylene Ether as Potentially CO2-neutral Fuel for Clean Diesel Engines Part 1: Engine Testing. *MTZ Worldw.* **2017**, *78*, 52–59. [CrossRef]
4. Dworschak, P.; Berger, V.; Härtl, M.; Wachtmeister, G. *Neat Oxymethylene Ethers: Combustion Performance and Emissions of OME_2, OME_3, OME_4 and OME_5 in a Single-Cylinder Diesel Engine*; SAE Technical Paper 2020-01-0805; SAE: Warrendale, PA, USA, 2020. [CrossRef]
5. Virt, M.; Arnold, U. Effects of Oxymethylene Ether in a Commercial Diesel Engine. *Cogn. Sustain.* **2022**, *1*. [CrossRef]
6. Pélerin, D.; Gaukel, K.; Härtl, M.; Jacob, E.; Wachtmeister, G. Potentials to simplify the engine system using the alternative diesel fuels oxymethylene ether OME1 and OME3-6 on a heavy-duty engine. *Fuel* **2020**, *259*, 116231. [CrossRef]
7. Omari, A.; Heuser, B.; Pischinger, S. Potential of oxymethylenether-diesel blends for ultra-low emission engines. *Fuel* **2017**, *209*, 232–237. [CrossRef]
8. Liu, J.; Wang, H.; Li, Y.; Zheng, Z.; Xue, Z.; Shang, H.; Yao, M. Effects of diesel/PODE (polyoxymethylene dimethyl ethers) blends on combustion and emission characteristics in a heavy duty diesel engine. *Fuel* **2016**, *177*, 206–216. [CrossRef]

9. Ma, Y.; Cui, L.; Ma, X.; Wang, J. Optical study on spray combustion characteristics of PODE/diesel blends in different ambient conditions. *Fuel* **2020**, *272*, 117691. [CrossRef]
10. Pastor, J.V.; García, A.; Micó, C.; Lewiski, F. Simultaneous high-speed spectroscopy and 2-color pyrometry analysis in an optical compression ignition engine fueled with OMEX-diesel blends. *Combust. Flame* **2021**, *230*, 111437. [CrossRef]
11. Damyanov, A.; Hofmann, P.; Geringer, B.; Schwaiger, N.; Pichler, T.; Siebenhofer, M. Biogenous ethers: Production and operation in a diesel engine. *Automot. Engine Technol.* **2018**, *3*, 69–82. [CrossRef]
12. Qiu, Z.; Zhong, A.; Huang, Z.; Han, D. An experimental and modeling study on polyoxymethylene dimethyl ether 3 (PODE3) oxidation in a jet stirred reactor. *Fundam. Res.* **2022**, *2*, 738–747. [CrossRef]
13. Gaukel, K.; Pélerin, D.; Härtl, M.; Wachtmeister, G.; Burger, J.; Maus, W.; Jacob, E. *Der Kraftstoff OME2: Ein Beispiel für den Weg zu emissionsneutralen Fahrzeugen mit Verbrennungsmotor/The Fuel OME2: An Example to Pave the Way to Emission-Neutral Vehicles with Internal Combustion En...*; VDI Verlag: Duesseldorf, Germany, 2016; pp. II-193–II-223. [CrossRef]
14. ECN. Engine Combustion Network. Available online: https://ecn.sandia.gov/ (accessed on 4 April 2024).
15. Pastor, J.V.; García-Oliver, J.M.; Micó, C.; García-Carrero, A.A.; Gómez, A. Experimental Study of the Effect of Hydrotreated Vegetable Oil and Oxymethylene Ethers on Main Spray and Combustion Characteristics under Engine Combustion Network Spray A Conditions. *Appl. Sci.* **2020**, *10*, 5460. [CrossRef]
16. Strauß, L.; Rieß, S.; Wensing, M. Mixture formation of OME3-5 and 1-Octanol in comparison with diesel-like Dodecane under ECN Spray A conditions. *Front. Mech. Eng.* **2023**, *9*, 1083658. [CrossRef]
17. Wiesmann, F.; Strauß, L.; Rieß, S.; Manin, J.; Wan, K.; Lauer, T. Numerical and Experimental Investigations on the Ignition Behavior of OME. *Energies* **2022**, *15*, 6855. [CrossRef]
18. Wiesmann, F.; Bauer, E.; Kaiser, S.A.; Lauer, T. *Ignition and Combustion Characteristics of OME_{3-5} and N-Dodecane: A Comparison Based on CFD Engine Simulations and Optical Experiments*; SAE Technical Paper 2023-01-0305; SAE: Warrendale, PA, USA, 2023. [CrossRef]
19. García-Oliver, J.M.; Novella, R.; Micó, C.; De Leon-Ceriani, D. Numerical analysis of the combustion process of oxymethylene ethers as low-carbon fuels for compression ignition engines. *Int. J. Engine Res.* **2023**, *24*, 2175–2186. [CrossRef]
20. Pastor, J.V.; García-Oliver, J.M.; Micó, C.; Tejada, F.J. Characterization of the oxymethylene ether fuels flame structure for ECN Spray A and Spray D nozzles. *Appl. Energy* **2023**, *332*, 120475. [CrossRef]
21. Kaario, O.T.; Karimkashi, S.; Bhattacharya, A.; Vuorinen, V.; Larmi, M.; Bai, X.S. A comparative study on methanol and *N*-Dodecane Spray Flames Using Large-Eddy Simulation. *Combust. Flame* **2024**, *260*, 113277. [CrossRef]
22. Sim, H.S.; Maes, N.; Weiss, L.; Pickett, L.M.; Skeen, S.A. Detailed measurements of transient two-stage ignition and combustion processes in high-pressure spray flames using simultaneous high-speed formaldehyde PLIF and schlieren imaging. *Proc. Combust. Inst.* **2021**, *38*, 5713–5721. [CrossRef]
23. ASG. ASG Analytik-Service. Available online: https://asg-analytik.de/ (accessed on 4 April 2024).
24. Tagliante, F.; Nguyen, T.M.; Dhanji, M.P.; Sim, H.S.; Pickett, L.M.; Manin, J.; Kukkadapu, G.; Whitesides, R.; Wan, K. The role of cool-flame fluctuations in high-pressure spray flames, studied using high-speed optical diagnostics and Large-Eddy Simulations. *Proc. Combust. Inst.* **2023**, *39*, 4871–4879. [CrossRef]
25. Higgins, B.; Siebers, D.L.; Aradi, A. *Diesel-Spray Ignition and Premixed-Burn Behavior*; SAE Technical Paper 2000-01-0940; SAE: Warrendale, PA, USA, 2000; ISSN 0148-7191. [CrossRef]
26. Reitz, R.D.; Beale, J.C. Modeling Spray Atomization with the Kelvin-Helmholtz/Rayleigh-Taylor Hybrid Model. *At. Sprays* **1999**, *9*, 623–650. [CrossRef]
27. Manin, J.; Bardi, M.; Pickett, L.; Payri, R. Boundary condition and fuel composition effects on injection processes of high-pressure sprays at the microscopic level. *Int. J. Multiph. Flow* **2016**, *83*, 267–278. [CrossRef]
28. CMT. Virtual Injection Rate Generator. Available online: https://www.cmt.upv.es (accessed on 4 April 2024).
29. Liang, L.; Stevens, J.G.; Farrell, J.T. A Dynamic Multi-Zone Partitioning Scheme for Solving Detailed Chemical Kinetics in Reactive Flow Computations. *Combust. Sci. Technol.* **2009**, *181*, 1345–1371. [CrossRef]
30. Niu, B.; Jia, M.; Chang, Y.; Duan, H.; Dong, X.; Wang, P. Construction of reduced oxidation mechanisms of polyoxymethylene dimethyl ethers (PODE1–6) with consistent structure using decoupling methodology and reaction rate rule. *Combust. Flame* **2021**, *232*, 111534. [CrossRef]
31. Nguyen, T.M.; Dahms, R.N.; Pickett, L.M.; Tagliante, F. The Corrected Distortion model for Lagrangian spray simulation of transcritical fuel injection. *Int. J. Multiph. Flow* **2022**, *148*, 103927. [CrossRef]
32. Pope, S.B. Ten questions concerning the large-eddy simulation of turbulent flows. *New J. Phys.* **2004**, *6*, 35. [CrossRef]
33. Senecal, P.K.; Pomraning, E.; Richards, K.J.; Som, S. *An Investigation of Grid Convergence for Spray Simulations Using an Les Turbulence Model*; SAE Technical Paper 2013-01-1083; SAE: Warrendale, PA, USA, 2013. [CrossRef]
34. Kundu, P.; Ameen, M.M.; Som, S. Importance of turbulence-chemistry interactions at low temperature engine conditions. *Combust. Flame* **2017**, *183*, 283–298. [CrossRef]
35. Kahila, H.; Wehrfritz, A.; Kaario, O.; Ghaderi Masouleh, M.; Maes, N.; Somers, B.; Vuorinen, V. Large-eddy simulation on the influence of injection pressure in reacting Spray A. *Combust. Flame* **2018**, *191*, 142–159. [CrossRef]
36. Hanjalić, K.; Popovac, M.; Hadžiabdić, M. A robust near-wall elliptic-relaxation eddy-viscosity turbulence model for CFD. *Int. J. Heat Fluid Flow* **2004**, *25*, 1047–1051. [CrossRef]

37. Durbin, P.A. Near-wall turbulence closure modeling without "damping functions". *Theor. Comput. Fluid Dyn.* **1991**, *3*, 1–13. [CrossRef]
38. Patel, V.C.; Rodi, W.; Scheuerer, G. Turbulence models for near-wall and low Reynolds number flows—A review. *AIAA J.* **1985**, *23*, 1308–1319. [CrossRef]
39. Brenn, G.; Deviprasath, L.J.; Durst, F. Computations and experiments on the evaporation of multi-component droplets. In Proceedings of the ICLASS 2003, Sorrento, Italy, 13–17 July 2003.
40. Reitz, R.D. Modeling atomization processes in high-pressure vaporizing sprays. *At. Spray Technol.* **1987**, *3*, 309–337.
41. O'Rourke, P.J.; Bracco, F. Modelling of Drop Interactions in Thick Sprays and a Comparison with Experiments. *IMECHE* **1980**, *404*, 101–116.
42. Amsden, A.A.; Butler, T.D.; O'Rourke, P.J. *The KIVA-II Computer Program for Transient Multidimensional Chemically Reactive Flows with Sprays*; SAE Technical Paper 872072; SAE: Warrendale, PA, USA, 1987. [CrossRef]
43. Schiller, L.; Naumann, A.Z. A Drag Coefficient Correlation. *Zeit. Ver. Deutsch. Ing.* **1933**, *77*, 318–320.
44. Liu, A.B.; Mather, D.; Reitz, R.D. *Modeling the Effects of Drop Drag and Breakup on Fuel Sprays*; SAE Technical Paper 930072; SAE: Warrendale, PA, USA, 1993. [CrossRef]
45. Pomraning, E.; Rutland, C.J. Dynamic One-Equation Nonviscosity Large-Eddy Simulation Model. *AIAA J.* **2002**, *40*, 689–701. [CrossRef]
46. Idicheria, C.A.; Pickett, L.M. *Formaldehyde Visualization Near Lift-off Location in a Diesel Jet*; SAE Technical Paper 2006-01-3434; SAE: Warrendale, PA, USA, 2006. [CrossRef]
47. Mueller, C.J. *The Quantification of Mixture Stoichiometry When Fuel Molecules Contain Oxidizer Elements or Oxidizer Molecules Contain Fuel Elements*; SAE Technical Paper 2005-01-3705; SAE: Warrendale, PA, USA, 2005. [CrossRef]
48. Maes, N.; Meijer, M.; Dam, N.; Somers, B.; Baya Toda, H.; Bruneaux, G.; Skeen, S.A.; Pickett, L.M.; Manin, J. Characterization of Spray A flame structure for parametric variations in ECN constant-volume vessels using chemiluminescence and laser-induced fluorescence. *Combust. Flame* **2016**, *174*, 138–151. [CrossRef]
49. Dahms, R.N.; Paczko, G.A.; Skeen, S.A.; Pickett, L.M. Understanding the ignition mechanism of high-pressure spray flames. *Proc. Combust. Inst.* **2017**, *36*, 2615–2623. [CrossRef]